Journal of Statistical Physics, Vol. 36, Nos. 5/6, 1984

Patterns of Energy Levels and Spectra for Polyatomic Molecules

William G. Harter[1,2]

1. INTRODUCTION

Laser spectroscopy has revealed a remarkable intricacy in the rotational, vibrational, and electronic energy levels for polyatomic molecules. The infrared spectra of SF_6,[1-10] CF_4,[11,12] and related molecules contain several levels of structure on top of structure which resembles a fractal in some ways. The purpose of this paper will be to exhibit some of this structure and introduce the simplest theoretical interpretations of it which are presently available.[13]

The theoretical interpretations are based upon quantum and semiclassical models for the dynamics of angular momenta for electronic and nuclear orbits and spins. The models show that very complex spectra can be understood in terms of comparatively simple nonlinear classical rotational dynamics combined with certain quantum tunneling processes.[14,15] The time scales for the classical and quantum motions vary over many orders of magnitude, and this accounts for the intricate structure of the molecular spectra.

Figure 1 represents an attempt to exhibit the complex spectral structure which can be seen using modern laser technology. Not too many years ago all this structure would have shown up only as a unresolved "landscape" on an infrared spectral trace, and it might have been called a vibrational "line" or "resonance." However, is quite clear from Fig. 1 that this "line" is actually made of many "sublines." Indeed, these lines contain lines which contain finer lines and so forth to yield a complex pattern with literally thousands of resonances.

One wonders what the SF_6 molecules could be doing to make all these spectral features. The designation "ν_4" refers to a particular type of dipole-

[1] Theoretical Division, Los Alamos National Laboratory, Los Alamos, New Mexico 87545.
[2] Presently on leave from the School of Physics and Center for Atomic and Molecular Studies, Georgia Institute of Technology, Atlanta, Georgia 30332.

0022-4715/84/0900-0749$03.50/0

822/36/5-6-16

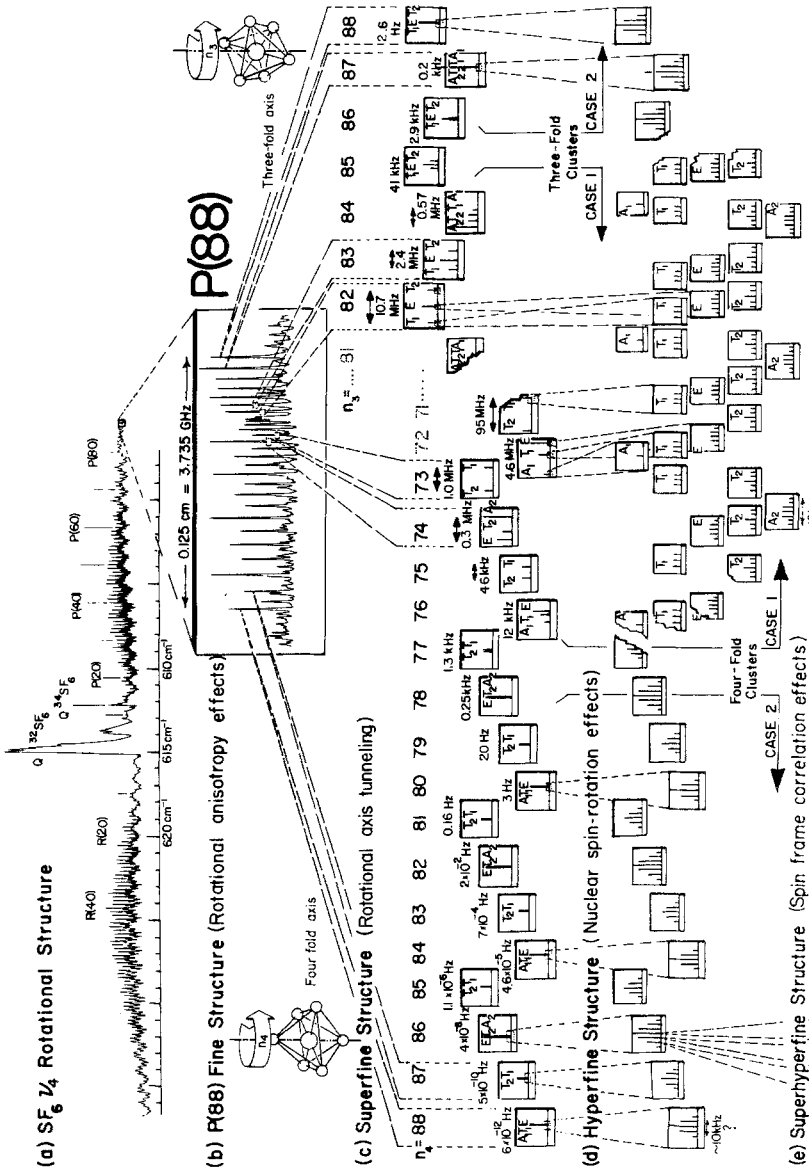

Fig. 1. A sampling of spectral patterns associated with the fundamental ν_4 vibrational transition of SF_6. (After Ref. 4). Parts a–e correspond to finer and finer spectral structure. An interpretation of some of the structure is attempted in the text.

active vibrational motion of the SF_6 molecule. All of the ν_4-spectral features in Fig. 1 correspond to an excitation of this vibration in one way or another. Still one wonders: Why can a ν_4 vibration be excited in so many different ways?

Much more clearly defined answers to such questions come out of a new approach to the study of rotations and angular momentum states of polyatomic molecules.[16] It was already known that the features in Fig. 1 correspond to transitions between states with different combinations or arrangements of angular momenta in the molecule. However, prevailing theories for spectroscopy lacked a clear geometric picture of how these angular momenta were arranged in each state, and there was no way to relate the complex spectra to a well-defined dynamics for the molecule.

There are three types of angular momentum involved in the ν_4 spectra. First, there are the angular momenta labeled **R**, **J**, or **F** associated with the overall rotation of the SF_6 molecule. Second, there is the vibrational angular momentum $\boldsymbol{l}$ associated with the eccentric or crankshaft-like motion of the ν_4 vibration.[14] Third, there is the total nuclear spin angular momentum **I** due to the six F nuclei which each have spin-1/2. The sum of the momentum **R** of the molecular rotor and the momentum $\boldsymbol{l}$ of the vibrator is the total mechanical momentum

$$\mathbf{J} = \mathbf{R} + \boldsymbol{l} \tag{1.1}$$

The overall total angular momentum

$$\mathbf{F} = \mathbf{J} + \mathbf{L} = \mathbf{R} + \boldsymbol{l} + \mathbf{I} \tag{1.2}$$

includes that of the nuclear spins, as well.

The new approach to the theory of rotational spectra is based upon the concept of the rotational energy (RE) surface as developed by Harter and Patterson.[13,14] In the following section this approach will be introduced for the simplest case in which vibrational and nuclear spin angular momentum effects are neglected ($\mathbf{R} = \mathbf{J} = \mathbf{F}$). This will allow a simple explanation of the spectral fine and superfine structures or cluster patterns which appear in Fig. 1b and c. Subsequent sections will show how these patterns are modified by other mechanisms such as Coriolis interaction with the vibrational momentum, higher-order tensor Hamiltonians, and nuclear spin effects. The effects of *electronic* spin and orbital coupling are not considered here, but it appears that they should be treated similarly.

2. ROTATIONAL ENERGY SURFACES AND SPECTRAL CLUSTERS

For molecules having a cubic, octahedral, or tetrahedral structure the following Hamiltonian form due to Hecht[17] has been extremely useful for modeling their rotational spectra:

$$H = BJ^2 + 10t_{044}[J_x^4 + J_y^4 + J_z^4 - (3/5)J^4] \tag{2.1}$$

The first term represents the rotational energy of a spherical top whose moment of intertia is $I = 1/(2B)$. The second term represents centrifugal distortion as explained below. The distortion term is the lowest degree polynomial in the angular momentum operators $(J_xJ_yJ_z)$ having cubic symmetry without also having spherical symmetry. (The second degree polynomial $J^2 = J_x^2 + J_y^2 + J_z^2$ in the first term obviously has spherical symmetry as well as cubic symmetry.)

The standard approach for solving Hamiltonians such as (2.1) involves rewriting them in terms of Racah tensors T_q^k. Following Hecht,[17] one rewrites the fourth-degree cubic part as follows:

$$J_x^4 + J_y^4 + J_z^4 - (3/5)J^4 = (2J^4/5)[T_0^4 + (5/14)^{1/2}(T_4^4 + T_{-4}^4)] \tag{2.2}$$

This is done so that matrix elements in an angular momentum basis can be derived easily using the Wigner–Eckart theorem:

$$\langle {}^{J'}_{K'} | T_q^k | {}^{J}_{K} \rangle = C^{kJJ'}_{qKK'} \langle J' \| k \| J \rangle \tag{2.3}$$

However, since most state for heavy polyatomic molecules involve high angular quanta $(J \geqslant 10)$ this approach becomes computationally laborious since many large matrices must be diagonalized numerically by computer. Also, the physical interpretation of the results of the diagonalizations are generally obscured, and important physical effects may be unnoticed or unexplained.

Computer diagonalization studies by Lea, Leask, and Wolf,[18] Dorney and Watson,[19] and Fox, Galbraith, Krohn, and Louck[20] revealed a complex yet surprisingly orderly cluster structure of the rotational energy levels. The first detailed explanation of the superfine structure of clusters was given by Harter and Patterson.[15,21] A much clearer explanation can be made by introducing the concept of the rotational energy surface.[13]

To obtain the rotational energy surface of a Hamiltonian such as (2.1) it is only necessary to plot it in an angular momentum polar coordinate system (β, γ) defined by the following:

$$\begin{aligned} J_x &= -J \sin\beta \cos\gamma \\ J_y &= J \sin\beta \sin\gamma \\ J_z &= J \cos\gamma \end{aligned} \tag{2.4}$$

Here the angles $(-\beta)$ and $(-\gamma)$ are the polar angles and azimuth, respectively, of the classical angular momentum vector $\mathbf{J} = (J_x J_y J_z)$ in the body frame of the molecule. The negative sign in this definition is convenient since the sense of rotation for the body frame is the reverse of that for the laboratory. Then angles $+\beta$ and $+\gamma$ are two of the conventionally defined Euler angles (α, β, γ) as explained in Ref. 13.

Using (2.4) to rewrite the Hamiltonian (2.1) one obtains

$$H = BJ^2 + t_{044}J^4(35\cos^4\beta - 30\cos^2\beta + 5\sin^4\beta\cos 4\gamma + 3)/2 \quad (2.5)$$

The polar plot of this function is shown by the surface in Fig. 2 for appropriate values of the constants B and t_{044}. (The location of features on the surface is independent of the values of these constants). One should remember that the energy is being plotted radially outward or upward. The

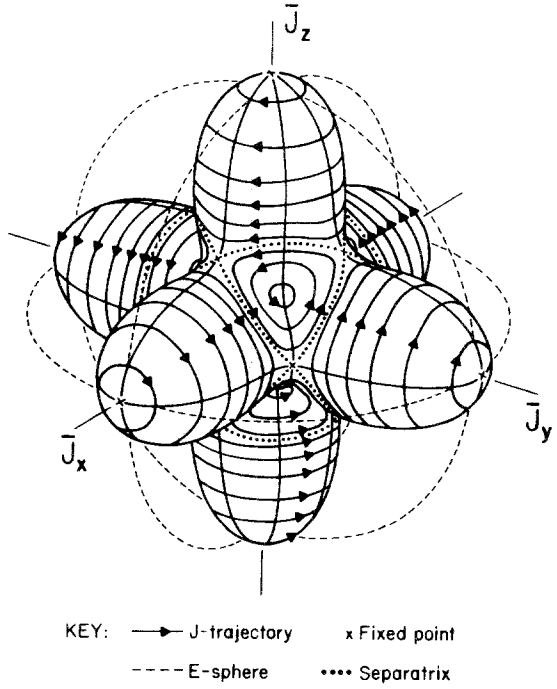

Fig. 2. The rotational energy (RE) surface for the SF_6 molecule. The rotationally energy is plotted radially as a function of the direction of the angular momentum **J**. Topography lines correspond to trajectories of the J vector precessing in the molecular frame with constant rotational energy. (At the same time **J** is a constant vector in the laboratory frame.) Dotted lines indicate separatrices, and dashed lines are constant energy tunneling paths on the E sphere.

radius of each point on the rotational energy (RE) surface represents the rotational energy obtained for the particular angular momentum direction $(-\beta, -\gamma)$ subject to the *constraint that the magnitude J of the angular momentum is constant.* It is often convenient to take unit values for J, i.e., to let

$$J = (J_x^2 + J_y^2 + J_z^2)^{1/2} = 1 \tag{2.6}$$

when plotting the classical surfaces.

It is useful to understand why the surface in Fig. 2 has peaks along the x, y, or z axes and valleys in between. It is helpful to imagine an octahedral SF_6 molecule with the S–F bonds along the same x, y, and z axes as Fig. 2. It often happens that an RE surface has a shape that is roughly similar to the molecule it is supposed to represent. [However, one should not forget that the RE surface exists in an *energy-angular momentum space* $(E, \mathbf{J})$, only.] If the SF_6 molecule rotates around the (100) directions (i.e., x, y, and z axes) it will be centrifugally distorted less than by rotation with the same J around (111) directions in between. This is because the radial S–F bonds are several times stronger than the F–F "bonds." Since centrifugal force acts perpendicular to the rotation axis or J vector, it will be more effective when J is not along the S–F axes but in between them. Greater distortion corresponds to greater effective rotational inertia and less energy, and so the RE surface has valleys on the (111) axes.

Therefore the RE surface is an effective energy surface that is supposed to account for the inertial deployment and shifting of cargo on board the molecule, as it rotates in space. It provides an efficient way to show the consequences of conservation of angular momentum (J) and energy (H). The constancy of J is implicit in the construction of the RE surface, and constant-H loci simply correspond to topography lines in Fig. 2. Since energy is plotted radially, the angular momentum vector $\mathbf{J}$ must lie along the intersections of an RE surface for a given J and an energy sphere for a given H. In the absence of external torque, the $\mathbf{J}$ vector must remain fixed in magnitude and direction in the laboratory, but in the body frame its direction (but not magnitude) will change as it moves along an RE surface topography line. This motion corresponds to an overall precesion or nutation of the molecule.

The speed or frequency of the precessional motion is determined by the gradient or slope of the energy surface. For each $\mathbf{J}$ vector position there is an angular velocity vector given by Hamilton's equation

$$\boldsymbol{\omega} = \frac{\partial H}{\partial \mathbf{J}} \tag{2.7}$$

and this determines the speed of **J** in the rotating body frame:

$$\dot{\mathbf{J}} = -\boldsymbol{\omega} \times \mathbf{J} \tag{2.8}$$

For qualitative purposes the following left-handed mnemonic is sufficient: the J vector precesses clockwise around RE surface maxima (left thumb up) and counterclockwise around minima. (The same rule applies to wind direction around highs or lows in the northern hemisphere.) The arrows on the topography lines in Fig. 2 indicate the directions of precession for each **J**-vector trajectory.

One of the most powerful features of an RE surface picture is that trajectories on the surface can often be related to quantum energy levels and spectral fine structure. In Fig. 3 the trajectories shown in Fig. 2 are associated with energy levels of SF_6 in the $J = R = 30$ vibrational ground state manifold. More precisely, the trajectories are associated with *clusters* of energy levels where the number of rotational levels in a given cluster equals the number of equivalent but distinct classical trajectories. For example, the third highest trajectories (...these are marked with arrows in the upper-right-hand side of Fig. 3) are associated with the third highest cluster of levels. The third circle from the lower-left-hand side of Fig. 3 displays a highly magnified view of a cluster of levels labeled E, T_1, and A_1. This cluster contains six levels altogether, as explained below.

The appearance of clusters in molecular spectra was one of the surprising revelations provided by modern laser spectroscopy.[20] Previously, the well-known group theory of quantum energy levels, established by Wigner and developed in dozens of textbooks, was supposed to account for all degeneracy due to symmetry of quantum energy levels. For example, levels labeled by octahedral symmetry species E and T_1 (or T_2) were understood to be doubly and triply degenerate, respectively, while species A_1 (or A_2) labeled single nondegenerate levels. A coincidence of any two or more symetry species in the absence of higher symmetry was often referred to as an "accidental degeneracy."

However, the near degeneracies of two-, three-, or four-symmetry species in the clusters indicated by Fig. 3 are clearly not accidents. In fact, the patterns of energy levels provide a direct comparison of classical vs. quantum mechanical behavior. The clusters are associated with a *classical* (or semiclassical) degeneracy of equivalent but disjoint trajectories for angular momentum precession. For example, each trajectory around one of the fourfold (C_4) symmetric peaks has the same energy as an equivalent one on each of the other five peaks. Each set of six classical trajectories corresponds to one of the C_4 clusters on the lower-right-hand side of Fig. 3. Each C_4 cluster has six rotational sublevels in the form of a $(T_1 T_2)$ or an

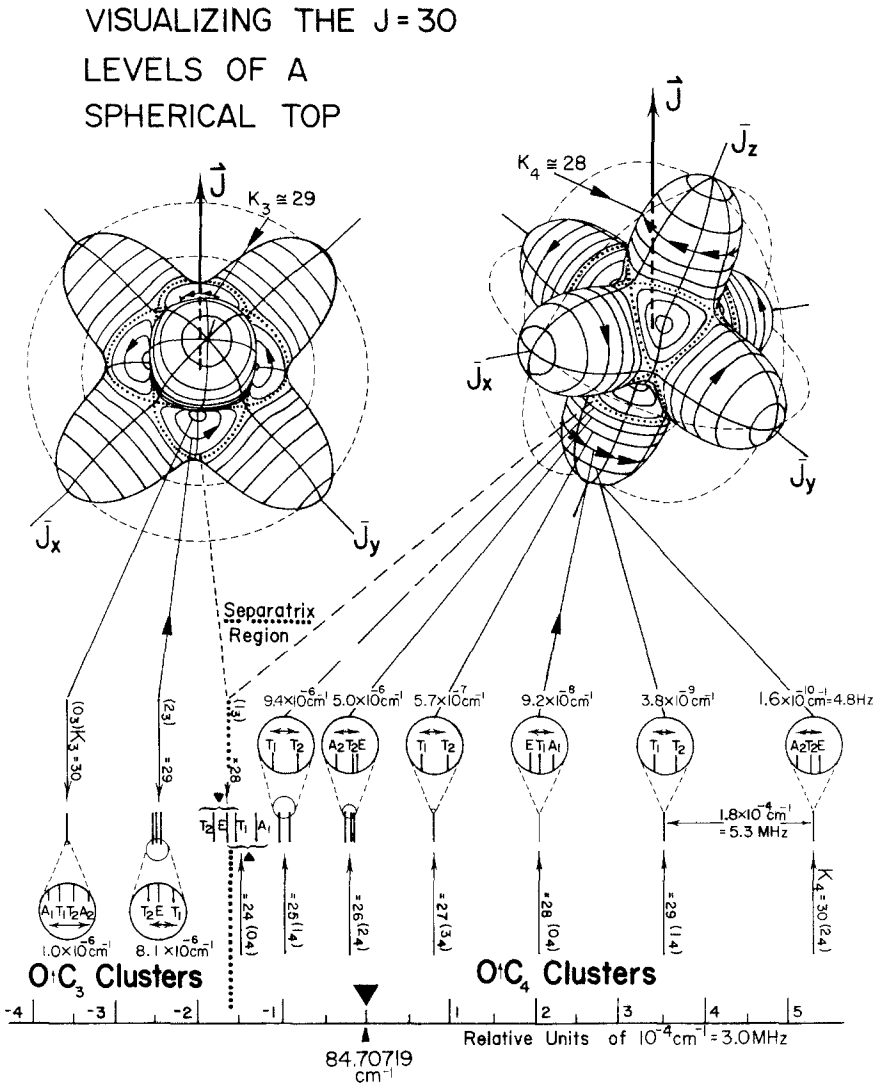

Fig. 3. Rotational energy level clusters of SF_6 for $J = 30$ are associated with RE surface trajectories of the precessing J vector. (After Ref. 13.) Rotational constants are $B = 0.091083\ \text{cm}^{-1}$ and $t_{044} = 5.44$ Hz. Spectrum is relative to $BJ(J+1)$.

(ATE) combination. On the right-hand side of Fig. 3 there are eight equivalent copies of each classical trajectory near the bottoms of threefold (C_3) symmetric valleys. Each set of eight corresponds to the same number of sublevels within C_3 clusters ($A_1T_1T_2A_2$) or (T_1ET_2).

The spacing and splitting of the clusters provides a direct measurement for the rates of classical versus quantum angular momentum dynamics. The rates for classical precessional motion are proportional to the intercluster spacing such as the ($1.8 \times 10^{-4}\ \text{cm}^{-1} = 5.3$ MHz) interval between the top two clusters in Fig. 3. The rates for quantum tunneling are proportional to the *intra*cluster splitting such as the ($1.6 \times 10^{-10}\ \text{cm}^{-1} = 4.8$ Hz) splitting of the top cluster in Fig. 3. Note that the classical precessional frequency for the top cluster is about a million times faster than the quantum tunneling frequency. This quantum tunneling frequency represents the rate for a classically impossible feat in which the molecule jumps from one equivalent precessional trajectory to another.

*Inter*cluster spacing in called *fine* structure splitting while the *intra*cluster splitting is called *super*fine structure splitting. Generally, the splitting of superfine structure is much finer than that of the "fine" structure since the corresponding quantum tunneling is much slower than the classical precession. However, if the different classical trajectories have points that are sufficiently near one another, then the quantum tunneling may become as rapid as the classical precession. This happens in what is called the *separatrix* or *saddle point* region of the energy space.

The dotted curves on the RE surface in Fig. 2 or 3 are called *separatrices*, and the separatrix segments connect saddle points. These dotted curves are called separatrices since they separate nearby trajectories which precess around different axes, and they lie on an energy sphere that passes through the saddle points. Equivalent but distinct trajejctories with energies slightly above or below the separatrix energy will form avoided crossings at each saddle point. In the neighborhood of the saddle point, the speed of the classical precession will be greatly reduced since the RE surface slope is nearly zero. However, the quantum tunneling will be greatly enhanced near these avoided crossings. Energy level clusters near the separtrix energy will have vanishing fine structure splitting since the classical precession rates are vanishing, but the tunneling frequency will suddenly blow up. In other words the cluster structure is completely melted away at the separatrix energy as can be seen in Fig. 3. The dynamics of a molecule near the separatrix energy may be extremely complicated and very sensitive to initial conditions. This has to be so since the separatrix marks the point where the molecule switches from C_3-type clusters and valley precession to a completely different C_4-type cluster and precession around peaks.

The C_3-cluster–separatrix–C_4-cluster structure is clearly visible in high-

resolution spectra. Probably the clearest and most beautiful examples so far are shown in laser spectra taken by Alan Pine[22] from cubane (C_8H_8). A ($J = 36$) example is shown in Fig. 4; it has a structure similar to that of ($J = 30$) levels in Fig. 3. The relative heights of the absorption peaks are determined by Pine from nuclear spin degeneracy and *not* simply by counting A, T, and E rotational degeneracies. A simple method for deriving XY_6 and XY_8 spin states was given by Harter and Patterson[16,23] and will be described briefly later.

In Fig. 1b there is an example of a $J = 88$ fine structure manifold of clusters with the details of the superfine structure shown below it in Fig. 1c. It is worth noting that Figs. 1 and 4 represent quantum *transitions* in vibrational spectra involving the rotational *levels* in Fig. 3. It will be shown in Section 5.2 that the relevant rotational energy surfaces for vibrationally excited states with large Coriolis interactions can have the same shapes as the basic surface shown in Fig. 2. In this case spectral structure is similar to level structure.

Before describing other types of RE surfaces we shall briefly mention an elementary semiclassical calculation of C_4-type fine and superfine energy levels.[13] This uses an Euler angle adaption of Bohr's original action quantization rule

$$A_n = \int_0^{2\pi} J_\gamma^+(E_n)\, d\gamma = 2\pi n, \qquad n = J, J-1, \ldots \tag{2.9}$$

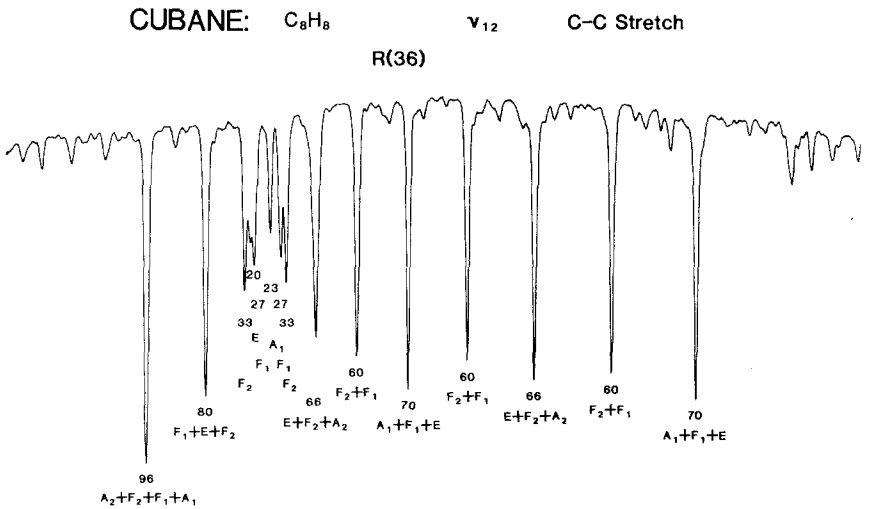

Fig. 4. Spectrum by Alan Pine of cubane C_8H_8 ν_{12} vibrational transition $R(36)$. (See Ref. 22.) Threefold clusters are separated from fourfold clusters by an uneven spectral separatrix region. Note that F symmetry labels in the figure are the same as T labels in the text.

where $J_y = J_z$ is the component of J about the C_4 axis of quantization found by solving (2.4) and (2.5), i.e.,

$$J_\gamma^{\pm} = \left\{ \frac{J^2(\cos^4\gamma + \sin^4\gamma) \pm [\varepsilon(\cos^4\gamma + \sin^4\gamma + 1) - J^4(\cos^4\gamma + \sin^4\gamma)]^{1/2}}{\cos^4\gamma + \sin^4\gamma + 1} \right\}^{1/2} \tag{2.10a}$$

where

$$\varepsilon = (E - BJ^2 + 3J^4/5)/10\, t_{044} \tag{2.10b}$$

For more accurate results one uses the quantum expectation values for angular momentum magnitudes, i.e., $J^2 \to J(J+1)$ and $J^4 \to [J(J+1)]^2$.

One varies the energy until the quantization condition (2.9) is satisfied. For $J = 30$ one obtains $E_n = 5.29,\ 3.53,\ 2.03,\ 0.79,\ -0.22,\ldots$ in units of $10^{-4}\ \mathrm{cm}^{-1}$. These compare well with the exact values of 5.31, 3.54, 2.04, 0.80, −0.20,... obtained by the lengthy procedure of numerical diagonalization. Note the classical precessional frequency (ν_c) is given by the well-known action derivative formula.

$$\nu_c = \left(\frac{\partial A_n}{\partial E_n}\right)^{-1} \simeq \frac{\Delta E}{\Delta n}\frac{\Delta n}{\Delta A} \simeq \frac{\Delta E}{h} \qquad (\text{for } \Delta n = 1) \tag{2.11}$$

This confirms the relation between ν_c and fine structure splitting ΔE.

The superfine splitting is determined by a tunneling amplitude

$$S = \nu_c e^{-|\theta|} \tag{2.12}$$

where

$$\theta = \int_{\text{path}} J_\gamma^-(E_n)\, d\gamma \tag{2.13}$$

is an integral over a saddle point. An example of such a path is the dashed path connecting the top C_4 trajectories around the J_x and J_y axes in Fig. 2. The limits of the tunneling integral are the closest approach points on the quantizing trajectories connected by a path. The tunneling amplitudes S appear in a tunneling matrix

$$\langle H \rangle = \begin{pmatrix} E & 0 & S & S & S & S \\ 0 & E & S & S & S & S \\ S & S & E & 0 & S & S \\ S & S & 0 & E & S & S \\ S & S & S & S & E & 0 \\ S & S & S & S & 0 & E \end{pmatrix} \begin{matrix} (100) \\ (-100) \\ (010) \\ (0\text{–}10) \\ (001) \\ (00\text{–}1) \end{matrix} \tag{2.14}$$

which connects the six equivalent C_4 trajectories that have energy E around the axes $\{(100), (-100),...\}$. The eigenvalues

$$h^{A_1} = E + 4S, \qquad h^{T_1} = E, \qquad h^E = E - 2S \tag{2.15}$$

of this matrix determine the superfine structure. Note that the T_1 level is twice as far from the A_1 level as the E level. This is what is observed in (ATE) clusters in spectra such as Figs. 1–4 where "nearest-neighbor" tunneling is the dominant quantum process. Other tunneling processes are discussed in Ref. 15.

3. SYMMETRY ANALYSIS FOR CLUSTERS OR SUPERFINE STRUCTURE

The symmetry analysis for spectral clusters may seem at first to be a little peculiar. Normally one expects a reduction in symmetry to cause the splitting of degenerate energy levels. For example, consider a reduction of cubic-octahedral (O) symmetry to C_4 symmetry by applying a z-magnetic field. This should cause the Zeeman splitting of the triply degenerate T_1 level into three levels of $m = 1, 0$, and -1. (The T_1 state is like an $l = 1$ p-type atomic orbital.)

Now a classical C_4-type cluster state with negligible tunneling also represents a reduction in symmetry if the molecule is stuck precessing on one of six C_4-symmetric trajectories. The molecule is adiabatically distorted from a perfect octahedron into something which really has no symmetry at all. At best it has a dynamical symmetry associated with a particular representation of the local C_4 symmetry of a single trajectory. However, the effect of this symmetry breaking on the spectrum is opposite to that of the Zeeman effect. Now the levels *un*split or cluster instead of splitting.

The difference is that in the Zeeman example the symmetry of the Hamiltonian was reduced artificially or externally. Clustering and many other related effects are associated with what should probably be called internal, spontaneous, or dynamical symmetry breaking. In the latter the symmetry of the underlying Hamiltonian is not disturbed, but at some point the wave function can be regarded as having collapsed or locked into one of several equivalent alternatives. This is a touchy point since this collapse cannot be brought about solely by Schrödinger dynamics. At some point a projection or "measurement" must be invoked. In the end the symmetry analysis and quantum mechanics must be made to produce localized wavepacket states that have "permanently" (for neglible tunneling) lost some of the symmetry they had before they were born. Something like this is need in order that a classical world can make its appearance. All classical entities

which we so take for granted such as nuclei, atoms, molecules, or chemical physicists must each have given up a considerable amount of symmetry in order to exist.

To understand the symmetry analysis for either type of symmetry breaking let us return to the C_4 Zeeman example. A well-known correlation exists between the octahedral representations and those of its subgroup C_4. Let us label the C_4 representations using azimuthal quanta-modulo-four, i.e., $[0_4, 1_4, 2_4, 3_4]$. For example, the T_1 representation is correlated with $m = 1 = 1_4$, $m = 0 = 0_4$, and $m = -1 = 3_4$ according to Zeeman splitting. The T_1 correlation is recorded in the T_1 row of the C_4 correlation table in Fig. 5 along with the other O representations. The rows of C_2 and C_3 tables provide similar correlations appropriate for the Zeeman-type applied symmetry breaking.

The remarkable thing about these tables is that the *columns* provide the necessary correlations for the clusters and spontaneous symmetry breaking. For example, the 0_4 column in Fig. 5 contains the cluster $(A_1 T_1 E)$. Whenever the azimuthal angular quantum number associated with a given quantizing C_4 trajectory is 0_4 (i.e., zero-modulo-four) then the $(A_1 T_1 E)$ cluster will be associated with that trajectory. This happens in Figs. 3 and 4 for $K_4 \simeq 36, 32, 28, 24,...$ and in Fig. 1 for $K_4 \simeq 88, 84,...$ etc. For odd values

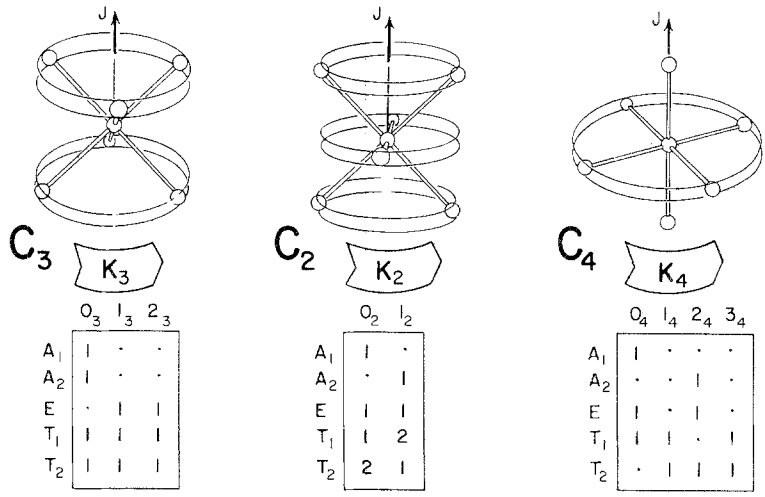

Fig. 5. Symmetry correlations for octahedral symmetry species and those of subgroups C_3, C_2, and C_4 (after Ref. 13). The subgroups are possible symmetries for classical trajectories on octahedral RE surface. The columns of each table give the number of each octahedral species involved in a particular type of cluster in Figs. 3, 4, 8, or 9. An XY_6 molecule is sketched rotating approximately as it would for each of the three subgroups. (Precessional motion is *not* being shown.)

of the azimuthal quantum number on C_4 trajectories the 1_4 or 3_4 cluster $(T_1 T_2)$ appears. The C_4 clusters correspond to the classical picture of SF_6 rotation sketched above the C_4 table. Similar analysis applies to the C_3 clusters using the C_3 table in Fig. 5. Examples of C_2 clusters will be shown in Section 5. Since the twofold axes in Figs. 2 and 3 contain saddles and separatrices, clustering is impossible there.

This symmetry analysis of clusters is based upon the theory of induced representations.[24] There are many new applications of this theory, but possibly none so prevalent and directly observable as in the rotational spectra of common polyatomic molecules. We briefly consider another application which helps to derive nuclear spin and hyperfine properties.

4. SYMMETRY ANALYSIS FOR NUCLEAR SPIN EFFECTS OR HYPERFINE STRUCTURE

A polyatomic molecule such as SF_6 or C_8H_8 can be regarded as undergoing spontaneous symmetry breaking in order to achieve its classical structure and cubic symmetry. Without this classical structure there is a much higher symmetry which includes the arbitrary interchange of the identical nuclei. The permutational symmetry S_6 of six identical F nuclei has $6! = 720$ operations and is 30 times larger than the cubic rotation group O, which has only 24 rotations. This corresponds to 30 equivalent choices for classical valleys into which the nuclear configuration could finally collapse in order to make a stable SF_6 molecule. The eight H nuclei must choose from 1680 equivalent final configurations around a cubic C_8 frame even if that frame is already established.

The correlation between the local cubic O symmetry representations and the much higher S_6 or S_8 representations is analogous to the correlation between C_4 symmetry and O representations in rotational cluster analysis. Table I is partial set of correlation tables appropriate for spin-1/2 nuclei F and H for S_4, S_6, and S_8 correlations with tetrahedral (T) and cubic (O) symmetry of XY_4, XY_6, and XY_8 molecules, respectively. The S_n representations are associated with Young spin tableaus which label the states of total nuclear spin $(I = 0, 1, 2,...)$ allowed by the Pauli exclusion principle.[16,23]

One notes that each O species is correlated with a supercluster of different nuclei spin states. For example, a T_1 state of cubane (C_8H_8) is correlated with five multiplets of total nuclear spin $I = 1$ and one each of spin $I = 2$ and 3 or 27 states altogether. T_2 is correlated with two $I = 0$ singlets, three each of $I = 1$ and $I = 2$ and one $I = 3$ septet or 33 states altogether. This explains the relative intensity values 27 and 33 written above

Table I. Correlation between Tetrahedral or Cubic Representations and Pauli-Allowed Total Nuclear Spin Quanta $I = 0, 1, \ldots, 4$

(a) $S_4 \downarrow T$

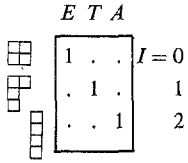

E	T	A	
1	.	.	$I=0$
.	1	.	1
.	.	1	2

(b) $S_6 \downarrow 0$

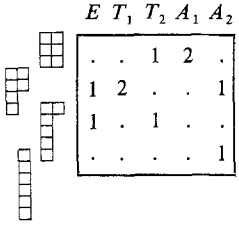

E	T_1	T_2	A_1	A_2	
.	.	1	2	.	$I=0$
1	2	.	.	1	1
1	.	1	.	.	2
.	.	.	.	1	3

(c) $S_8 \downarrow 0$

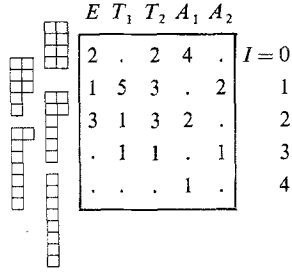

E	T_1	T_2	A_1	A_2	
2	.	2	4	.	$I=0$
1	5	3	.	2	1
3	1	3	2	.	2
.	1	1	.	1	3
.	.	.	1	.	4

the T_1 and T_2 lines in Pine's spectrum in Fig. 4. (Note: T means the same as F.)

The absorption peaks associated with clusters have relative intensities which are the sums of those of their constituents. For example, the $(T_1 T_2)$ clusters have relative intensity $(27 + 33 = 60)$. However, the effect of clustering and related rotational dynamics on spin states is much more subtle than this. As the cluster splitting or S becomes smaller the nature of the nuclear spin state may be drastically altered. Symmetry species which normally are prohibited from mixing can be strongly mixed and total nuclear spin (I) may no longer be a good quantum number. This can happen whenever the superfine splitting is comparable to or less than the hyperfine, i.e., less than about 20 kHz.

Since the superfine splitting drops exponentially according to (2.12) there can be many clusters in which hyperfine mixing of species plays a major role. These are called *case 2* clusters in Fig. 1d. It is clear that many case 2 clusters exist. Using extraordinary laser techniques Christian Bordé[3,25,26] has observed many examples of hyperfine mixing in case 2 clusters in SF_6. Jacques Bordé[25,26] has verified the effects in detailed computer studies. These experiments open a new era in the study of molecular structure and dynamics.

The dynamics of nuclear spins in the presence of nonlinear rotational dynamics needs to be analyzed in more detail. The detailed spectra of strong case 2 clusters as well as borderline case 1–case 2 clusters need to be understood. Preliminary studies include the use of case $1 \rightarrow 2$ correlation diagrams such as Fig. 6, and approximate quantum models of the resulting energy levels.[14] The resulting spectral patterns are called superhyperfine

structure in Fig. 1e and should lead to many interesting effects involving nuclear spin–rotation coupling and RE surface dynamics.

We consider now some related effects involving some different kinds of RE surface dynamics and vibration–rotation coupling.

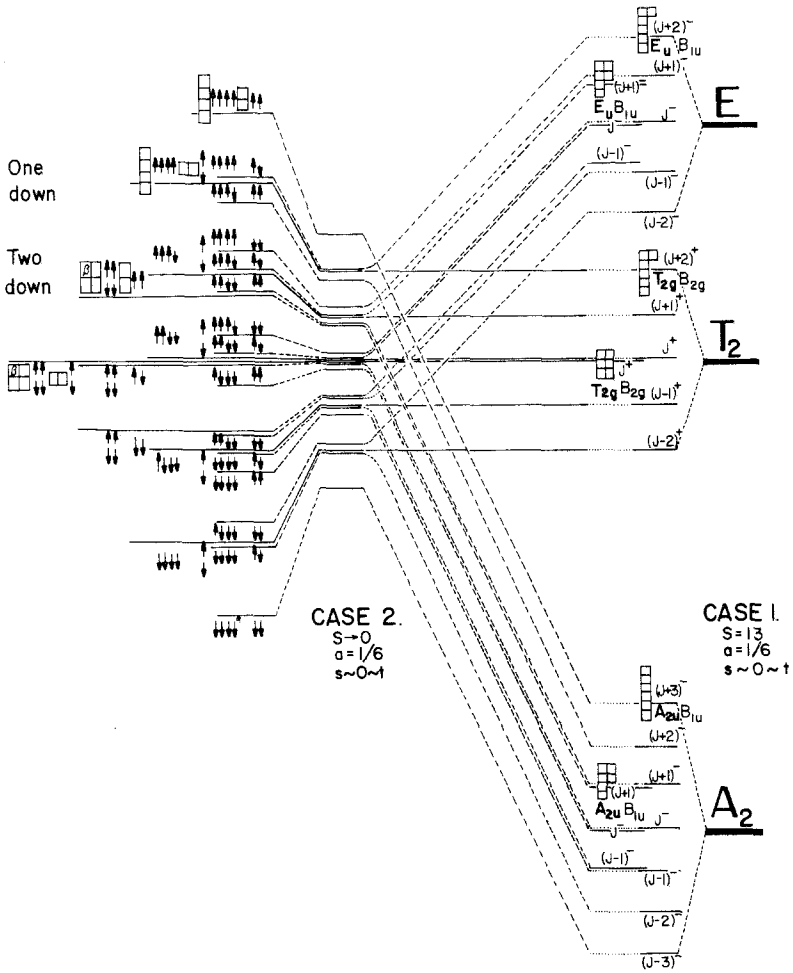

Fig. 6. SF_6 hyperfine structure within an (A_2T_2E) cluster (after Ref. 14). The hyperfine multiplets associated with A_2, T_2, and E are sketched on the right-hand side. (They follow from Table Ib.) As the RE surface tunneling amplitude S vanishes the three multiplets are drawn together and the symmetry species become mixed. The resulting spectrum is called superhyperfine or case 2 structure. (See also Fig. 1d and e.)

5. OTHER TYPES OF RE SURFACES AND SPECTRAL PATTERNS

We consider now some different possibilities for RE surfaces and their resulting spectral patterns. These represent only a few of the many interesting effects that can be discovered using RE surface pictures and they should be observable in laser spectra of polyatomic molecules.

5.1. Fourth- and Sixth-Rank Tensor Combinations

The RE surfaces and spectra of the combination tensor

$$T^{4,6}(v) = \hat{T}^4 \cos v + \hat{T}^6 \sin v \tag{5.1}$$

will be displayed for a range of values for the mixing parameter $v = 0$, $\pi/6,..., \pi$. The first term involves a normalized fourth-rank tensor proportional to the one given in Eqs. (1.1), (2.2), and (2.5):

$$\begin{aligned}\hat{T}^4 &= (7/12)^{1/2}[T_0^4 + (5/14)^{1/2}(T_4^4 + T_{-4}^4)] \\ &= (21/2^{10}\pi)^{1/2}(35\cos^4\beta - 30\cos^2\beta + 5\sin^4\beta\cos 4\gamma + 3)\end{aligned} \tag{5.2}$$

The second term is a normalized sixth-rank tensor which also has cubic symmetry:

$$\begin{aligned}\hat{T}^6 &= (1/8)^{1/2}[T_0^6 - (7/2)^{1/2}(T_4^6 + T_{-4}^6)] \\ &= (13/2^{13}\pi)^{1/2}(231\cos^6\beta - 315\cos^4\beta + 105\cos^2\beta \\ &\quad - 21\sin^4\theta(11\cos^2\theta - 1)\cos 4\gamma - 5)\end{aligned} \tag{5.3}$$

One may plot each $T^{4,6}$ for a given v as an RE surface as was done in Fig. 2 for the $v = 0$ case.[27] However, plotting in the spherical geometry can make it difficult for one's eye to spot saddle points or other flat regions. Therefore we shall borrow a technique from world maps and plot the rotational energy along the z axis above a stereographic projection of roughly half the unit sphere. The x and y coordinates on the projected plane will be given in terms of the polar angles β and γ by

$$\begin{aligned}x &= \tan(\beta/2)\cos(\gamma) \\ y &= \tan(\beta/2)\sin(\gamma)\end{aligned} \tag{5.4}$$

Thus the equator ($\beta = \pi/2$) becomes a unit circle in the x–y plane. (In fact, any circle on the sphere is mapped into a circle or straight line on the x–y plane.)

The $T^{4,6}$ RE surfaces are plotted as functions of x and y ($-1.0 \leqslant x$, $y \leqslant 1.0$) for several values of v in Fig. 7. The plots are 3D (three-

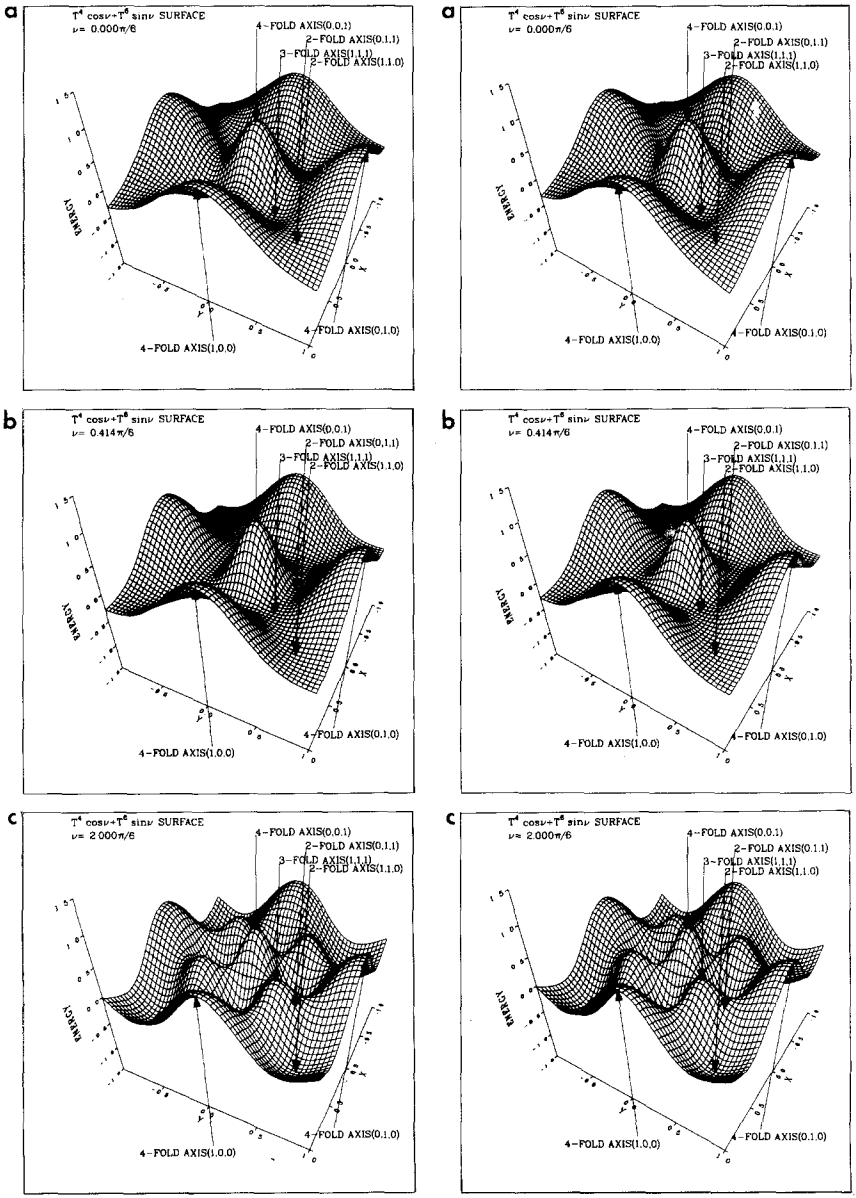

Fig. 7. Rotational energy (RE) surfaces for mixed tensor $T^{4,6} = T^4 \cos v + T^6 \sin v$ for various values of mixing angle v. Surface coordinates are projected according to Eq. (5.4) onto x and y base plane. Drawings are 3D stereo pairs, and should be so viewed to see axis positions. (a) The $v = 0$ surface corresponds to Fig. 2, (b) $v = 0.4138(\pi/6)$, (c) $v = 2(\pi/6)$, (d) $v = 4(\pi/6)$, (e) $v = 4.6478(\pi/6)$, (f) $v = \pi$.

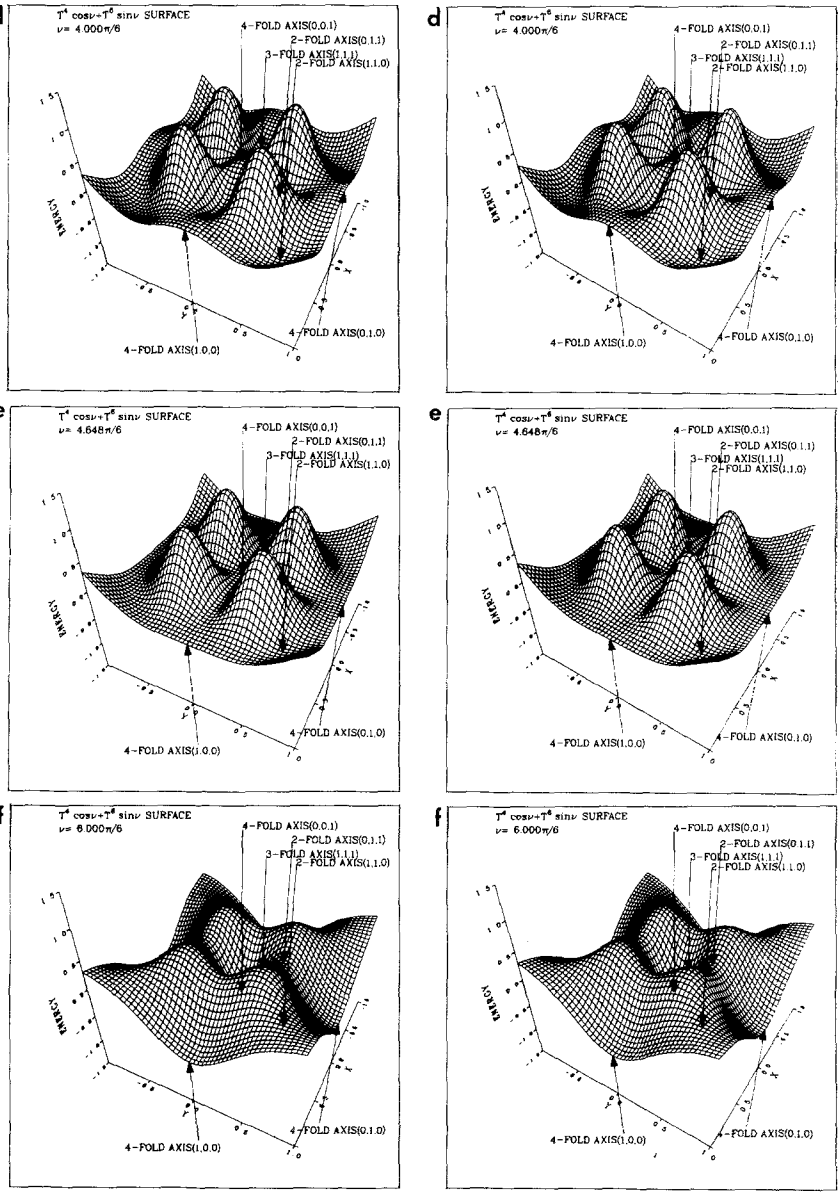

Fig. 7 (*continued*)

dimensional) stereo drawings which can be viewed by relaxing the eyes so that the left and right eyes see the left and right images, respectively. A stereo viewer or a card held between the drawings may help one enjoy the 3D views more easily. One should first examine the $v = 0$ drawing in Fig. 7a which represents the top half of the RE surface in Fig. 2. Note the peaks on fourfold axes, valleys on threefold axes, and saddles on twofold axes. The contours of Fig. 2 are not reproduced on Fig. 7, but one can see approximately where they would go since the constant energy surfaces in Fig. 7 are *planes* parallel to x and y.

Next one should examine the $v = 2.0(\pi/6)$ surface in Fig. 7c. It is clear that the twofold axes no longer have saddle points but have developed fairly deep valleys. This means that some topography lines or classical trajectgories will encircle the twofold axes, and that $T^{4,6}$ operators with approximately the same v will have twofold clusters. These are of the form $(A_1 E T_1 T_2 T_2)$ or $(A_2 E T_1 T_1 T_2)$ obtained from the columns of the C_2 table in Fig. 5, and each have 12 rotational sublevels altogether.

The eigenvalues of $T^{4,6}$ for $J = 30$ are plotted as a function of v $(0 \leqslant v \leqslant \pi)$ in Fig. 8 below. At $v = 0$ the spectrum has the same form as in Fig. 3, but it quickly changes as v varies. Clusters trade species and form

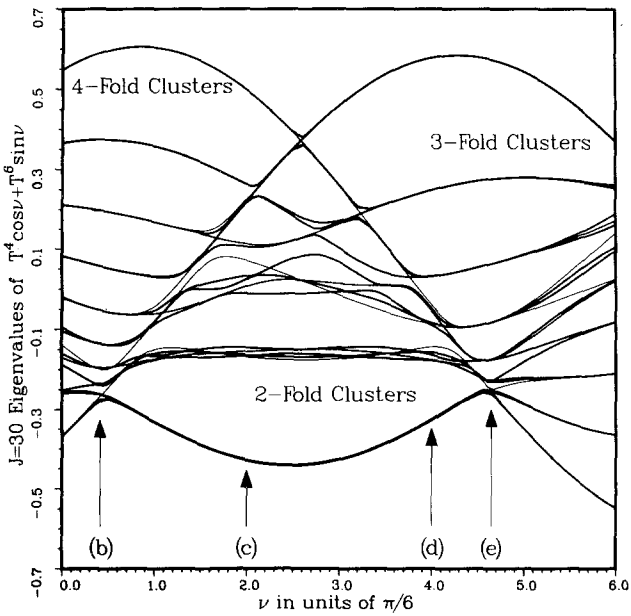

Fig. 8. Energy levels for mixed tensor $T^{4,6} = T^4 \cos v + T^6 \sin v$ as a function of mixing angle v for $J = 30$. (After Ref. 27.) The $v = 0$ or $v = \pi$ levels are similar to those in Fig. 3. The arrows indicate the levels corresponding to RE surfaces in Figs. 7b, c, d, and e, respectively.

new clusters including a pair of twofold clusters that go from about $\nu = 0.4(\pi/6)$ to about $\nu = 4.6(\pi/6)$ in the lower center portion of Fig. 8. The superfine structure of the upper one is visible without magnification. Twelve states in five levels are crowded together in these clusters.

The surfaces at the values $\nu = 0.414(\pi/6)$ and $\nu = 4.648(\pi/6)$ where the twofold clusters begin and end are shown in Fig. 7b or e. These are values for which the twofold energy equals the energy at the three or fourfold axes, respectively. From Fig. 8 one can see that the energy spectrum is dominated at these points by four- or threefold clusters, respectively. Finally, one should note that the $\nu = \pi$ surface in Fig. 7f is just an upside-down version of the $\nu = 0$ surface in Fig. 7a.

The pattern of changing geography and eigenvalues seen in Figs. 7 and 8 will be similar to that which occurs in a much more complicated Coriolis coupling problem discussed in the following section.

5.2. Scalar and Tensor Coriolis Combinations

The fundamental ν_3 and ν_4 vibrational states are each spanned by a dipole active triplet of vectorlike base states $\{\phi_1^1, \phi_0^1, \phi_{-1}^1\}$ of vibrational angular momentum $l = 1$ and cubic symmetry species T_1. The coupling of the vibrational angular momentum l with the rotational momentum R yields a total angular momentum $J = R + l$ which is conserved. In SF_6 and other similar molecules most of the angular momentum coupling or Coriolis effects are well described by the following Hamiltonian[28]:

$$H_v = v + BJ^2 + 2B\zeta \mathbf{J} \cdot \mathbf{l} + t_{224}[v^2(\text{rotation} \times v^2(\text{vibration})]^4_{A_1} \qquad (5.5)$$

where the first two terms determine the vibrational and rotational energy, and the second two terms determine the vibration–rotation or Coriolis interactions.

We shall compare the spectra and RE surface dynamics of the interactions by varying the coefficient $\beta\zeta$ (B-zeta) of the scalar Coriolis operator for a fixed value of the tensor coefficient t_{224}. We shall once again treat the angular momentum as a semiclassical quantity which precesses around topgraphy lines on an RE surface. The problem is: What RE surface?

This is a new approach to Coriolis effects, but a useful analogy can be made with older problems. Jahn, Teller, and Renner studied electron-vibration vibronic interactions involving two, three, or more electronic basis functions $\{\phi_1, \phi_2, \phi_3, ...\}$ with the same or nearly the same energy. As is well known this degeneracy signals a possible "breakdown" of the Born–Oppenheimer approximation and the whole system of electrons and vibrating

nuclei can become "floppy." To study the dynamics of such a system one constructs n multiple interpenetrating potential energy (PE) surfaces by diagonalizing an effective Hamiltonian in the electronic basis $\{\phi_1, \phi, ..., \phi_n\}$ as a function of vibrational coordinates.

To study the Coriolis dynamics we shall similarly diagonalize an effective Hamiltonian in the body-defined basis

$$\{|\Pi_1\rangle = \phi_1, \qquad |\Sigma\rangle = \phi_0, \qquad |\Pi_{-1}\rangle = \phi_{-1}\}$$

of *vibrational* functions and plot the three resulting functions of the angular momentum direction angles $\{\beta, \gamma\}$ or the projected $\{x, y\}$ coordinates given by (5.4). This will yield three sometimes interpenetrating RE surfaces which will provide information about Coriolis dynamics and spectra.

The details of the derivation of the effective Hamiltonian is mostly described in Ref. 28 and cannot be repeated here owing to lack of space. The result in the $\{\Pi\Sigma\}$ body basis is the following (here we ignore v and BJ^2):

$$\begin{array}{c} \\ \langle H\rangle_{\text{body}} = 2t_{224}J^2 \\ \\ \\ + 2B\zeta J \end{array} \begin{array}{c} \begin{array}{ccc} |\Pi_1\rangle & |\Sigma\rangle & |\Pi_{-1}\rangle \end{array} \\ \begin{pmatrix} 3\cos^2\beta - 1 & -2\sqrt{2}\sin\beta\cos\beta(\cos\gamma - i\sin\gamma) & \sin^2\beta(6\cos 2\gamma + i4\sin 2\gamma) \\ \text{cc.} & -2(3\cos^2\beta - 1) & 2\sqrt{2}\sin\beta\cos\beta(\cos\gamma - i\sin\gamma) \\ \text{cc.} & \text{cc.} & 3\cos^2\beta - 1 \end{pmatrix} \\ \\ \begin{pmatrix} \cos\beta & \sin\beta(\cos\gamma - i\sin\gamma)/\sqrt{2} & 0 \\ \text{cc.} & 0 & \sin\beta(\cos\gamma - i\sin\gamma)/\sqrt{2} \\ \text{cc.} & \text{cc.} & -\cos\beta \end{pmatrix} \end{array} \tag{5.6}$$

For many purposes it is more convenient to have this matrix in the laboratory-defined basis. We shall designate the lab basis by

$$\{|P\rangle = |R = J + 1\rangle, \qquad |Q\rangle = |R = J\rangle, \qquad |R\rangle = |R = J - 1\rangle\}$$

in correspondence with the P, Q, and R branches of a v spectrum (see Fig. 1a) which result from transitions to these states when $B\zeta$ is much larger than t_{224}. In this representation the scalar Coriolis operator $J \cdot l$ is diagonal,

$$\begin{array}{c} \\ \langle H\rangle_{\text{lab}} = \\ \\ \\ \times \end{array} \begin{array}{c} \begin{array}{ccc} |P\rangle & |Q\rangle & |R\rangle \end{array} \\ \begin{pmatrix} 2B\zeta J & 0 & 0 \\ 0 & 0 & 0 \\ 0 & 0 & -2B\zeta J \end{pmatrix} + 2t_{224}J^2 \\ \\ \begin{pmatrix} H_{PP} & H_{PQ} & H_{PR} \\ H_{PQ}^* & H_{QQ} & H_{QR} \\ H^* & H_{QR}^* & H_{RR} \end{pmatrix} \end{array} \tag{5.7}$$

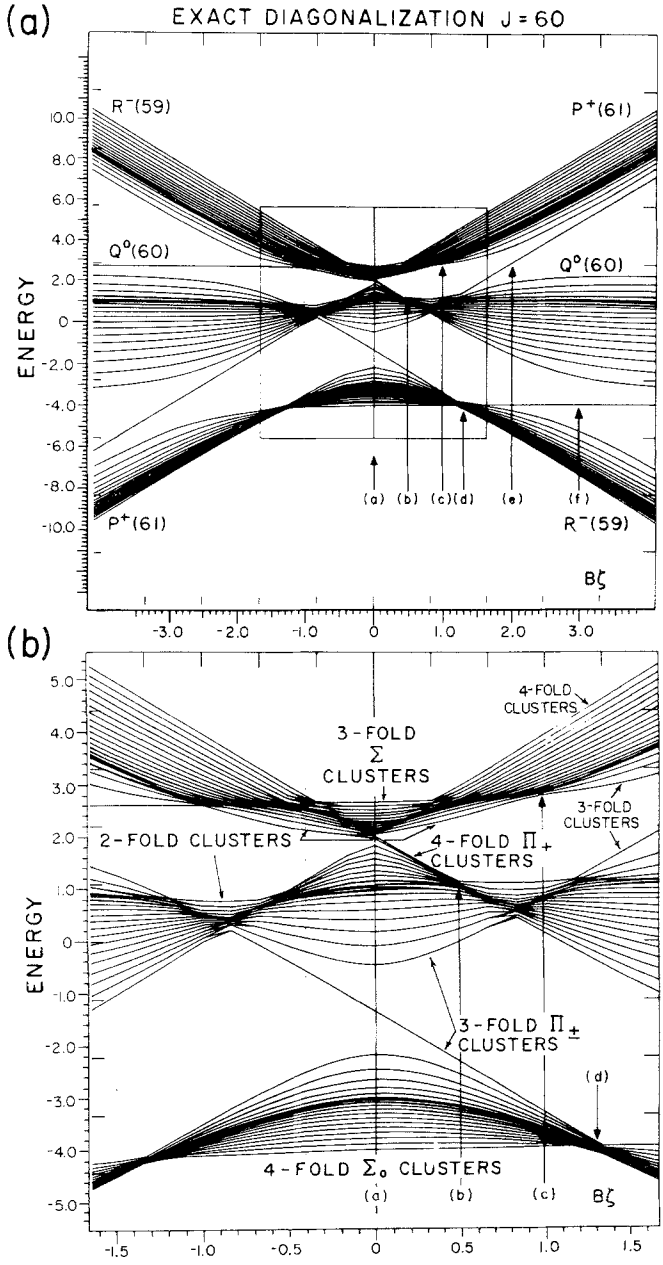

Fig. 9. Energy levels for unit fourth-rank tensor Coroilis operator as a function of scalar Coriolis coefficient $B\zeta$. Part of the (a) figure is magnified in (b) to show the structure around $B\zeta = 0$. The arrows indicate levels corresponding to RE surfaces in Fig. 10a, b, c, d, e, and f, respectively.

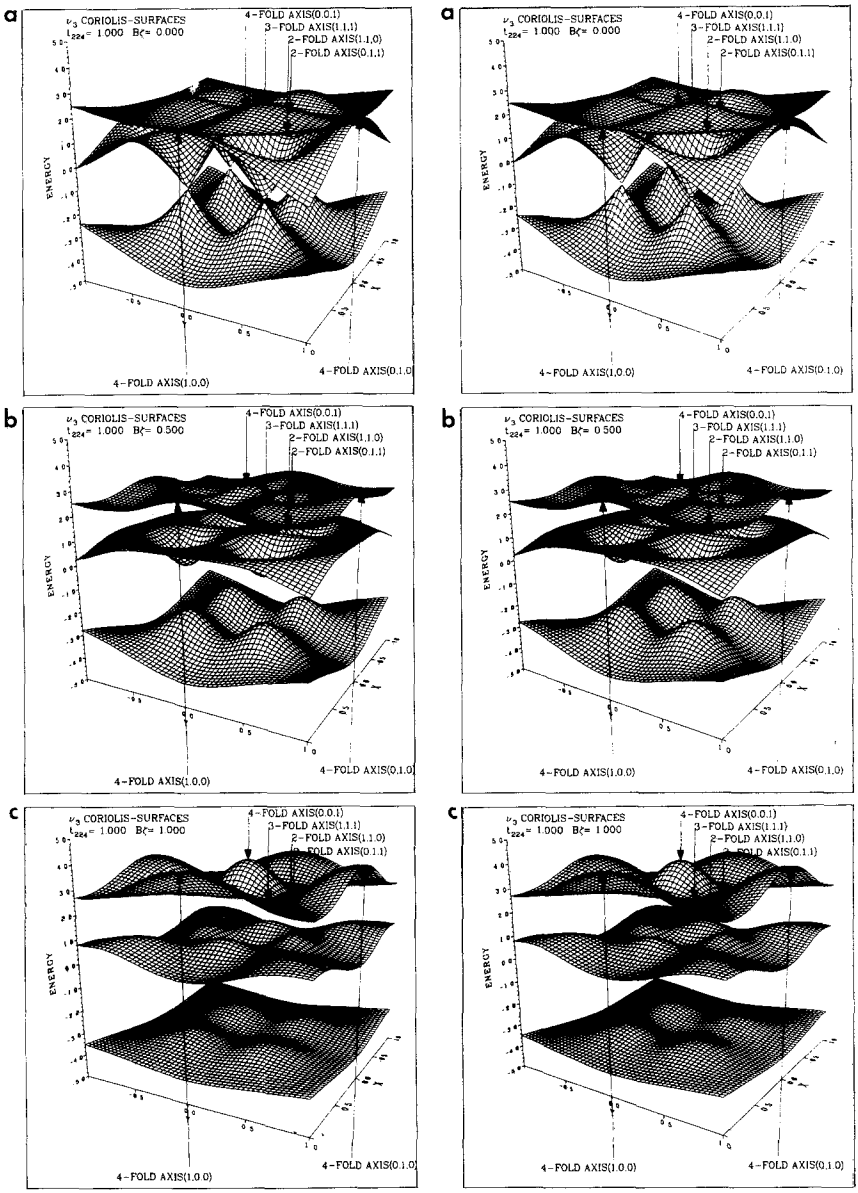

Fig. 10. Rotational energy (RE) surfaces for unit fourth-rank tensor Coriolis operator for various values of scalar Coriolis coefficient $B\zeta$: (a) $B\zeta = 0$, (b) $B\zeta = 0.5$, (c) $B\zeta = 1.0$, (d) $B\zeta = 1.3$, (e) $B\zeta = 2.0$, (f) $B\zeta = 3.0$.

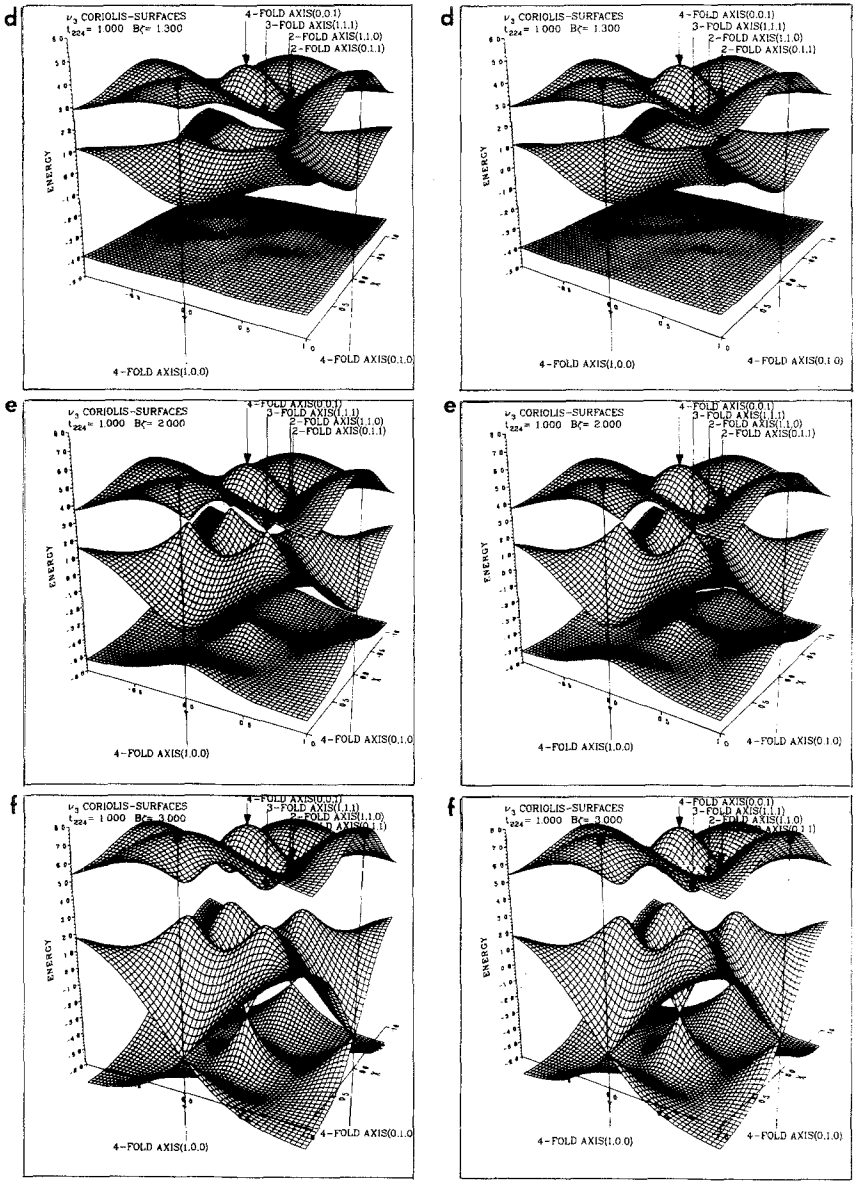

Fig. 10 (*continued*)

and the tensor Coriolis components are given as follows:

$$H_{PP} = H_{RR} = (35\cos^4\beta - 30\cos^2\beta + 5\sin^4\beta\cos 4\gamma + 3)/4$$
$$= -H_{QQ}/2 \tag{5.8}$$
$$H_{PQ} = 5\sin\beta[7\cos^3\beta - 3\cos\beta - \sin^2\beta(\cos\beta\cos 4\gamma + i\sin 4\gamma)]/2\sqrt{2}$$
$$= -H_{QR} \tag{5.9}$$
$$H_{PR} = 5[-7\cos^4\beta + 8\cos^2\beta + (1-\cos^4\beta)\cos 4\gamma$$
$$+ 2i\cos\beta\sin^2\beta\sin 4\gamma - 1]/4 \tag{5.10}$$

One should note that the diagonal components (5.8) have precisely the form of the $(l=0)$ ground level RE surface defined by (2.5). The excited $(l=1)$ level RE surfaces consist of three copies of ground level RE surface with the middle (Q) one upside down and twice as deep for large $B\zeta$. Then the rotor angular momentum $\mathbf{R}$ is mostly conserved and provides a good quantum number $R = J+1$, J, or $J-1$ for well separated P, Q, and R branches. The vibrational momentum l is defined by its component on the lab fixed J vector.

It is interesting to see what happens when $B\zeta$ is small or zero. A plot of the resulting spectrum for $J=60$ is shown in Fig. 9a and b. Figure 9b presents a magnified view of the neighborhood of $B\zeta = 0$.

One should note that the upper branch of level trajectories in Fig. 9b has a pair of triangular regions which contain twofold clusters for $B\zeta > 0$ and $|B\zeta| \leqslant 1.2$. Each triangular region is surrounded on its upper side by regions containing mostly threefold clusters on one side and mostly fourfold clusters on the other side and separatrix regions in between. In other words, each triangular region in Fig. 9b resembles the triangular region the middle of Fig. 8 which is due to sixth-rank tensors having produced stable twofold clusters. This was quite surprising to find in the spectra of a fourth-rank tensor which generally has only unstable saddle points on twofold axes. How then can stable classical rotation be established on a twofold axis for small $B\zeta$?

The 3D plots of RE surfaces in Fig. 10 show clearly that stable valleys or peaks exist on twofold axes for low values of $B\zeta$. The Coriolis interaction can stabilize an otherwise unstable motion just as a magnetic field can stabilize orbits in a quadrupole ion trap. Comparison of the top surface in the first two plots in Fig. 10 (for $B\zeta = 0.0$ and $B\zeta = 0.5$) reveals that the latter has developed valleys on the twofold axis. The top surface for $B\zeta = 0.0$ resembles the $v = 4.6(\pi/6)$ surface in Fig. 7e and supports threefold clusters only. The middle surface for $B\zeta = 0.5$ (Fig. 10b) has the same shape only upside down, and it corresponds to the lower limit for stable twofold

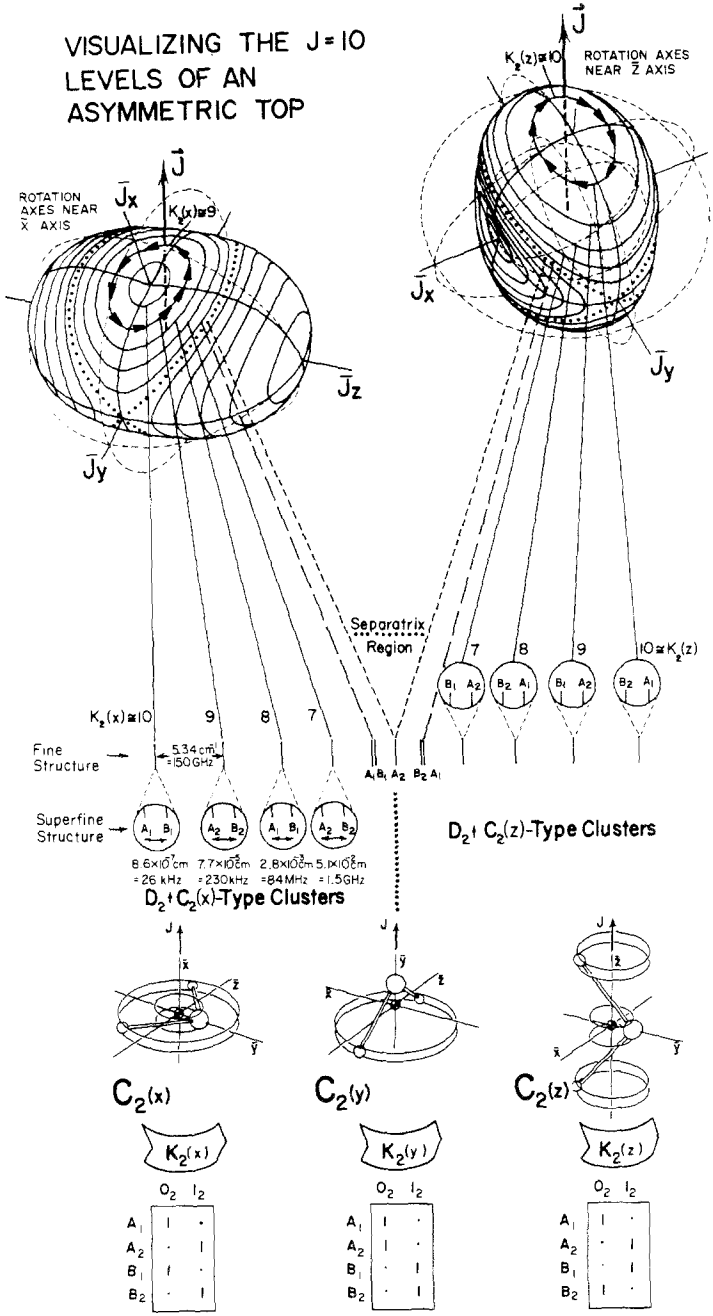

Fig. 11. Rotational energy level clusters for a rigid asymmetric top for $J = 10$ are associated with RE surface trajectories (see Ref. 13). Correlations between the asymmetric top symmetry D_2 and three dynamical subgroups $C_2(x)$, $C_2(y)$, and $C_2(z)$ are shown below the level-cluster diagram. (Recall analogous Figs. 3 and 5 for octahedral clusters.)

precession on this surface. The top surface with $B\zeta = 1.0$ (Fig. 10c) has a shape similar to the $v = 0.41(\pi/6)$ surface in Fig. 7b. It supports only fourfold precession and corresponds to the upper limit for twofold precession on the top surface. However, at $B\zeta = 1.0$ the twofold clusters are still very strong in the middle region as seen in Figs. 9b or 10c.

By comparing Figs. 9 and 10 for various values of $B\zeta$ it is seen that very complicated spectral patterns are described quite simply and accurately by the RE surface pictures even in the presence of resonant Coriolis mixing at small $B\zeta$. Furthermore, each point on the surface corresponds to a particular eigenstate combination of vibrational states $\{|\Pi_1\rangle\,|\Sigma\rangle\,|\Pi_{-1}\rangle\}$ or else $\{|P\rangle\,|Q\rangle\,|R\rangle\}$. The former are body-defined angular momentum states which will be more convenient bases to use in the limit of $B\zeta = 0$, i.e., when the Born–Oppenheimer approximation for vibrational wavefunctions is valid.

Other interesting points of comparison between spectra in Fig. 9 and RE surfaces in Fig. 10 include $B\zeta \cong 1.3$ when the lower surface is almost flat, and crossover points or conical intersections at $B\zeta = 2.0$ and 3.0. The physical interpretation of these patterns and dynamics must await future work.

5.3. Twofold Clusters in Asymmetric Tops

As a final example we show the $J = 10$ energy levels and RE surface trajectories for an asymmetric rigid top in Fig. 11. This example shows that absence of high symmetry does not necesarily prevent the existence of cluster patterns and semiclassical analysis. The details of the asymmetric top analysis are discussed in Ref. 13 and are based upon earlier work by King[29] and Colwell, Handy, and Miller.[30] The twofold or $C_2(x)$ and $C_2(y)$ clusters in Fig. 11 are analogous to the C_3 and C_4 clusters for the octahedral symmetry in Fig. 3. The $C_2(y)$ clusters are impossible when the y-axis sits on saddle points. SF_6 (or C_8H_8) and asymmetric tops represent two extremes in molecular symmetry. Between these extremes there shjould be a broad range of molecules with fascinating examples of spectral patterns and rovibronic dynamics. A clear picture of this dynamics can be obtained from analysis of rotational energy surfaces.

ACKNOWLEDGMENTS

I would like to thank Alan Pine for copies of the cubane spectrum, and the National Science Foundation for partial support from Grant No. PHY-8207150 in theoretical physics.

REFERENCES

1. J. P. Aldridge, H. Filip, H. Flicker, R. F. Holland, R. S. McDowell, N. G. Nereson, and K. Fox, *J. Mol. Spectrosc.* **58**:165 (1975).
2. R. S. McDowell, H. W. Galbraith, C. D. Cantrell, N. G. Nereson, and E. D. Hinkley, *J. Mol. Spectrosc.* **68**:288 (1977).
3. Ch. J. Bordé, M. Ouhayoun, A. Van Lerberge, C. Saloman, S. Avrillier, C. D. Cantrell, and J. Bordé, *Laser Spectroscopy IV*, H. Walther and K. W. Rothe, eds. (Springer, New York, 1979).
4. K. C. Kim, W. B. Person, D. Seitz, and B. J. Krohn, *J. Mol. Spectrosc.* **76**:322 (1979).
5. P. F. Moulton, D. M. Larsen, J. N. Walpole, and A. Mooradian, *Opt. Lett.* **1**:51 (1977).
6. C. W. Patterson, R. S. McDowell, P. F. Moulton, and A. Mooradian, *Opt. Lett.* **6**:93 (1981).
7. A. S. Pine and A. G. Robiette, *J. Mol. Spectrosc.* **80**:388 (1980).
8. C. W. Patterson, B. J. Krohn, and A. S. Pine, *J. Mol. Spectrosc.* **88**:133 (1981).
9. C. Reiser, J. I. Steinfeld, and H. W. Galbraith, *J. Chem. Phys.* **74**:2189 (1981).
10. M. Dubs, D. Harradine, E. Schweitzer, and J. I. Steinfeld, and C. W. Patterson, *J. Chem. Phys.* **77**:3824 (1982).
11. R. S. McDowell, M. J. Reisfeld, H. W. Galbraith, B. J. Krohn, H. Flicker, R. C. Kennedy, J. P. Aldrige, and N. G. Nereson, *J. Mol. Spectrosc.* **83**:440 (1986).
12. M. Takami, *J. Chem. Phys.* **73**:2665 (1980); **72**:4276 (1981); **76**:1670 (1982).
13. W. G. Harter and C. W. Patterson, *J. Chem. Phys.* **80**:4241 (1984).
14. W. G. Harter, *Phys. Rev. A* **24**:192–263 (1981).
15. W. G. Harter and C. W. Patterson, *J. Chem. Phys.* **66**:4872 (1977).
16. W. G. Harter, C. W. Patterson, and F. J. daPaixao, *Rev. Mod. Phys.* **50**:37 (1978).
17. Karl T. Hecht, *J. Mol. Spectrosc.* **5**:355 (1960).
18. K. R. Lea, M. J. M. Leask, and W. P. Wolf, *J. Phys. Chem. Solids* **23**:1381 (1962).
19. A. J. Dorney and J. K. G. Watson, *J. Mol. Spectrosc.* **42**:1 (1972).
20. K. Fox, H. W. Galbraith, B. J. Krohn, and J. D. Louck, *Phys. Rev. A* **15**:1363 (1977).
21. W. G. Harter and C. W. Patterson, *Phys. Rev. Lett.* **38**:224 (1977).
22. A. S. Pine, A. G. Maki, A. G. Robiette, B. J. Krohn, J. K. G. Watson, and Th. Urbanek, *J. Am. Chem. Soc.* **106**:891 (1984).
23. W. G. Harter and C. W. Patterson, in *Group Theoretical Methods in Physics*, W. Beiglboch *et al.*, eds., Lecture Notes in Physics No. 94 (Springer, New York, 1979), p. 80.
24. S. L. Altman, *Induced Representations in Crystals and Molecules* (Academic Press, New York, 1977).
25. J. Bordé, Ch. J. Bordé, C. Salomon, A. Van Lerberghe, M. Ouhayoun, and C. C. Cantrell, *Phys. Rev. Lett.* **45**:14 (1980).
26. J. Bordé and Ch. J. Bordé, *Chem. Phys.* **71**:417 (1982).
27. W. G. Harter and C. W. Patterson, *J. Math. Phys.* **20**:1453 (1979).
28. W. G. Harter, C. W. Patterson, and H. W. Galbraith, *J. Chem. Phys.* **69**:4896 (1978).
29. G. W. King, *J. Chem. Phys.* **15**:820 (1947).
30. S. M. Colwell, N. C. Handy, and W. H. Miller, *J. Chem. Phys.* **68**:745 (1978).